

# On the structural composition and stability of Fe–N–C catalysts prepared by an intermediate acid leaching

Ulrike I. Kramm<sup>1,4</sup> · Alessandro Zana<sup>2</sup> · Tom Vosch<sup>2</sup> · Sebastian Fiechter<sup>3</sup> · Matthias Arenz<sup>2</sup> · Dieter Schmeißer<sup>1</sup>

Received: 10 July 2015 / Revised: 12 October 2015 / Accepted: 16 October 2015 / Published online: 28 October 2015  
© Springer-Verlag Berlin Heidelberg 2015

**Abstract** The development of highly active and stable non-noble metal catalysts (NNMC) for the oxygen reduction reaction (ORR) in proton exchange membrane fuel cells (PEM-FC) becomes of importance in order to enable cost reduction. In this work, we discuss the structural composition as derived from Fe-57 Mößbauer spectroscopy and X-ray diffraction, catalytic performance determined by a rotating (ring) disk electrode (RRDE) technique and stability evaluation of our Fe–N–C catalysts prepared by an intermediate acid leaching (IAL). The advantage of this IAL is given by a high density of active sites within the catalyst, as even without sulphur addition, an iron carbide formation and related disintegration of active sites are inhibited. In addition, our accelerated stress tests illustrate better stability of the sulphur-free IAL catalyst in comparison to the sulphur-added one.

**Keywords** Non-noble metal catalysts (NNMC) · Fe–N–C · ORR · PEM-FC · Accelerated stress tests (ASTs) · Mößbauer spectroscopy

## Introduction

For a sustainable society, fossil fuels have to be stepwise replaced by renewable energy sources. While for the stationary energy supply, several good solutions are available, additional research is needed for automotive propulsion. The application of proton exchange membrane fuel cells (PEM-FC) for the conversion of chemical energy stored in hydrogen and oxygen to electric energy is a promising solution, and recent years have seen great advances in the commercial sector. However, for long-term and mass application, the amount of precious metal used in PEM-FC has to be reduced to be competitive with commercial combustion engines [1]. Non-noble metal catalysts hold the promise of being able to completely avoid precious metals in PEM-FC. As in standard PEM-FCs, the largest quantity of precious metal is required to catalyze the oxygen reduction; current research concentrates on this reaction. In order to be applicable, a new catalyst has to be cheap in costs and has to reach high volumetric catalytic activity in order to replace platinum-based catalysts. In recent years, the number of publications on Me–N–C catalysts, especially iron-based ones, has significantly increased. Based on different spectroscopic techniques, the general understanding on the active site structure [2–15] and additional factors affecting the oxygen reduction reaction (ORR) activity [5, 16–20] has become clearer. As a result, there are currently several preparation approaches that enable ORR activities that are close to the D.O.E. target value [9, 21–24]. Catalysts prepared by the oxalate-supported pyrolysis of porphyrins reach outstanding ORR activity in rotating disk electrode (RDE)

Dedicated to Jose Zagal on the occasion of his 65th birthday

**Electronic supplementary material** The online version of this article (doi:10.1007/s10008-015-3060-z) contains supplementary material, which is available to authorized users.

✉ Ulrike I. Kramm  
kramm@ese.tu-darmstadt.de

<sup>1</sup> Department of Physics, BTU Cottbus-Senftenberg, Konrad-Wachsmann-Allee 17, 03046 Cottbus, Germany

<sup>2</sup> Nano-Science Center, Department of Chemistry, University of Copenhagen, Universitetsparken 5, 2100 Copenhagen, Denmark

<sup>3</sup> Institute for Solar Fuels, Lise-Meitner-Campus of the Helmholtz-Center Berlin, Hahn-Meitner-Platz 1, 14109 Berlin, Germany

<sup>4</sup> Graduate School of Excellence Energy Science and Engineering, Departments of Chemistry and Materials- and Earth-Science, TU Darmstadt, Jovanka-Bontschits-Str. 2, 64287 Darmstadt, Germany

experiments and very good performance during PEM-FC application [25]. To our knowledge, it was the first preparation approach to yield Me–N–C catalysts without the utilization of a carbon black [26]. Therefore, higher densities of active sites and related current densities can be yielded as demonstrated for today's most active Fe–N–C catalysts [9, 22, 27].

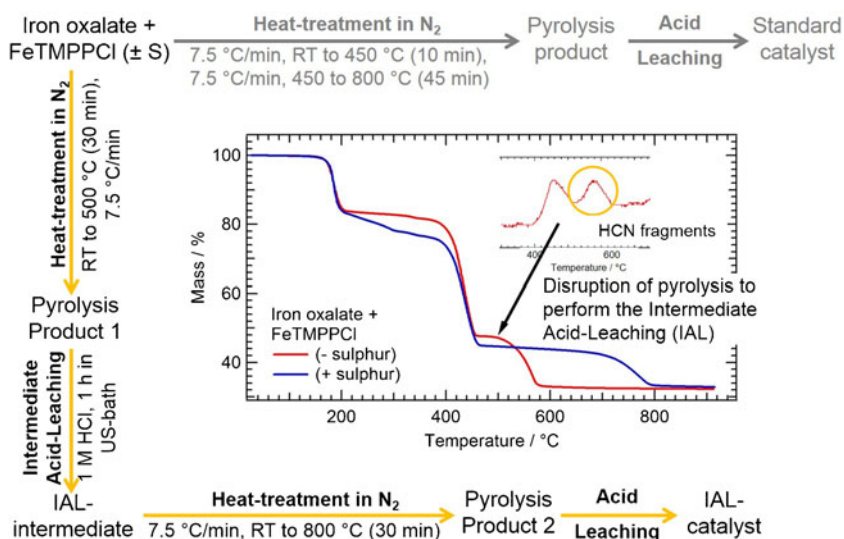
In order to optimize the ORR activity, sulphur was added to the precursor mixture [28, 29]. However, a possible drawback of this approach might be sulphur poisoning, a phenomenon known for Pt/C catalysts [30]. Furthermore, the carbon morphology of the catalysts prepared by the oxalate-supported pyrolysis under sulphur addition is highly amorphous, which seems to contradict a good oxidative stability in PEM-FC tests. In our recent work [29], we have shown that during the synthesis of Fe–N–C catalysts, the formation of iron carbide (at 550–600 °C) is accompanied by the decomposition of FeN<sub>4</sub> centres (expressed by the release of HCN fragments in TG-MS, compared also Fig. 1), consequently limiting the ORR activity. There are two strategies to avoid the active site destruction: first, addition of sulphur to the precursor mixture prior to the heat treatment step [2, 28, 31] and, second, performing an intermediate acid leaching (IAL) [29]. Our previous approach was related to the addition of sulphur to the porphyrin + iron oxalate mixtures. With this strategy, one can gain one order of magnitude higher kinetic current densities in comparison to the sulphur-free catalysts. The drawbacks are (i) the presence of sulphur residuals in the catalyst (as possible poison during PEM-FC application), (ii) the in situ formation of a highly amorphous carbon and (iii) the fact that sulphur addition is only applicable for preparation temperatures up to 800 °C. Above this temperature, sulphur addition cannot prevent the iron carbide formation as indicated by thermodynamic calculations (see Fig. S1) and confirmed by previous results obtained from high-temperature X-ray diffraction (HT-XRD).

Our alternative (improved) approach, namely performing an IAL after a pre-heat treatment to 500 °C, prevents all these drawbacks, as the approach is applicable also to precursors without any sulphur. In this work, we present a detailed structural analysis of these catalysts.

In addition to this, so far, all non-noble metal catalysts (NNMC) fail in terms of long-term stability. In this respect, long-term measurements in PEM-FC [32] or accelerated stress tests (ASTs) in aqueous electrolyte [10, 33–36] are helpful for a better understanding.

For the application of ORR catalysts in PEM-FC, they have to fulfil requirements with respect to the standard operation conditions in a “low-potential window” ( $U < 1.0$  V) and a “high-potential window”, respectively. As shown by Reiser et al. [37], during start-up and shutdown, oxygen can penetrate the anode catalyst layer, with the consequence of oxygen reduction in those regions of the anode. In order to equilibrate this significant potential change on the anode, also the cathode potential will increase to a value of 1.3–1.7 V. Hence, high potential excursion up to 1.5 V (reversible hydrogen electrode (RHE)) can take place in a PEM-FC system during the start-up and shutdown of the membrane electrode assembly (MEA). Given a standard oxidation potential of ca. 0.207 V for carbon, the potential window applied during this AST can significantly accelerate the carbon corrosion as demonstrated for Pt/C catalysts [35]. The impact of carbon corrosion on MEA systems is severe and can lead to a significant performance loss. In the case of Pt/C catalysts, carbon corrosion can induce agglomeration, sintering and loss of surface area within the catalyst layer and, thus, a thinning of it [37, 38]. While the first two degradation modes are specific of supported catalysts, the last phenomenon can indeed be fatal for Fe–N–C catalyst [32]. Here, the surface area correlates well with ORR activity as the active sites are either integrated in the graphene layers or bridging adjacent graphene edges [7, 9, 17]. Hence, carbon

**Fig. 1** Preparation scheme for the oxalate-supported pyrolysis in order to reach the “Standard catalysts” (route indicated by grey arrows) and the adapted route to yield the IAL intermediates and IAL catalysts via intermediate acid leaching synthesis (yellow arrows)



corrosion will consequently lead to a disintegration of active sites. Indeed, in a recent report by Goellner et al., a carbon loss due to corrosion of <20 % led to an activity decay of 90 % [10]. Moreover, for the investigated catalyst, the activation energy for carbon oxidation was determined to be  $E_A = 38 \text{ kJ mol}^{-1}$ . Consequently, when applied at 80 °C, a 14-fold higher carbon corrosion is expected compared to room temperature [10]. Own post-mortem analysis of MEAs equipped with Fe–N–C cathode layers and subjected to an oxidizing treatment in PEM-FC showed a decrease of the catalyst layer mass by 66 %. This was due to carbon oxidation (major part) and leaching of iron sites (minor), whereas the change of iron content correlated well with the change in metal content [32]. Ferrandon et al. investigated the so far most stable Fe–N–C catalysts by post-mortem and in situ X-ray absorption near edge spectroscopy (XANES) measurements [39]. While the catalysts performed stable over 200 h of potentiostatic operation at 0.4 V in PEM-FC, they found a significant change in iron concentration (–84 %) and iron coordination. This large loss in iron concentration without significant impact on ORR activity is due to a high concentration of inorganic iron sites in the particular catalyst. The simultaneous observation of stable performance and significant loss of iron was interpreted by the authors with a balance of the deactivation of active sites and re-utilization of active sites that were previously hidden in the bulk [39].

In order to test the ability of the two catalysts used in this work to withstand such high potential excursion, we adopt an AST treatment given by the Fuel Cell Conference, Japan (FCCJ), that simulates the potential excursion felt by the cathode during start-up and shutdown [40].

In addition to this, the performance of the catalysts under standard operation conditions was tested (<1.0 V), AST\_Run. These results will be addressed in the second part of the paper; the first is directed to the structural characterization of the catalysts prepared by IAL.

## Experimental part

### Catalyst synthesis

The synthesis protocol of standard catalysts and IAL catalysts is visualized in Fig. 1. The preparation of the standard catalyst was similar to the route described elsewhere [29]. Shortly, defined amounts of 1.3 mmol FeTMPPCL and 28.6 mmol iron oxalate dihydrate (without and with sulphur (1.2 mmol  $\text{S}_8$ )) were heated continuously up to 800 °C in inert gas atmosphere. After cooling down, the obtained product was acid-leached in 1 M HCl for 1 h, filtrated and rinsed with water, and the catalyst powder was dried overnight.

The IAL catalysts were prepared by a multi-step synthesis approach. The same precursor mixtures as for the standard

catalysts were heated up to 500 °C in inert gas, followed by the IAL in 1 M HCl for 1 h. After filtration, rinsing with water and drying the IAL intermediates were subjected again to a heat treatment, this time up to 800 °C, and after cooling down to room temperature (RT), the Pyrolysis Product 2 was again subjected to an acid leaching in 1 M HCl for 1 h. After filtration, rinsing with water and drying the IAL catalysts were obtained.

It should be pointed out that the molar ratio of FeTMPPCL to iron oxalate dihydrate (and sulphur in the case of the +S catalyst) was similar for IAL catalysts and standard catalysts. Most of the characterization described in this work was made on the final IAL catalysts; in some cases, measurements of the IAL intermediates or Pyrolysis Product 2 were added, too.

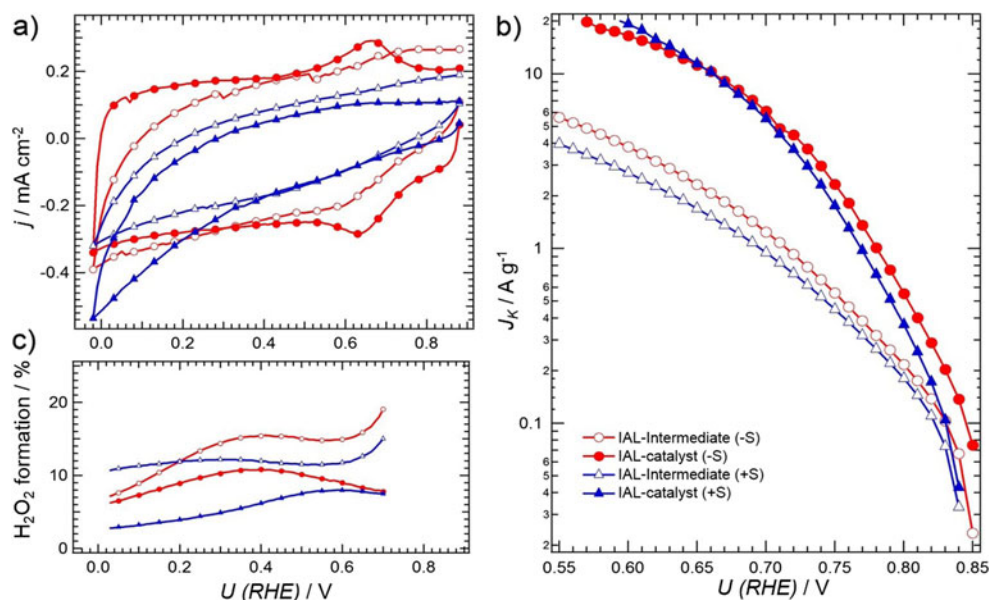
### Characterization

**Electrochemistry** The conditions for measuring the ORR activity and selectivity (“Characterization of the intermediate acid leaching catalysts” section) of IAL catalysts and IAL intermediates were different compared to those applied in “Stability in accelerated stress test” section evaluating the stability of the IAL catalysts.

For measuring the ORR activity and selectivity (“Characterization of the intermediate acid leaching catalysts” section), a catalyst loading of  $0.13 \text{ mg cm}^{-2}$  with a Nafion to catalyst ratio of 2:5 was placed onto the glassy carbon disc ( $A = 0.1963 \text{ cm}^2$ ) of a rotating (ring) disk electrode (RRDE) with a platinum ring. The experiments were carried out at RT in a three-electrode system with a platinum wire as counter electrode and  $\text{Hg/Hg}_2\text{SO}_4/0.5 \text{ M H}_2\text{SO}_4$  as reference electrode (0.68 V vs. RHE). In the first step, the working electrode was cycled in a potential range of 1.0 to 0.0 V with a scan rate of  $50 \text{ mV s}^{-1}$  in nitrogen-saturated  $0.5 \text{ M H}_2\text{SO}_4$ . Typically, 15–20 scans were required until a steady state was reached. In the cyclic voltammetry (CV) diagrams of Fig. 2a, always the last scans out of this line are displayed. The platinum ring was activated by continuous cycling in a potential range of 0.0 to 1.65 V until a steady state was reached. Previous to the RRDE experiments, the electrolyte was purged with oxygen and the open circuit potential (OCP) was measured. The experiments were performed with a sweep rate of  $5 \text{ mV s}^{-1}$  in oxygen-saturated electrolyte at 200, 400, 576, 729 and 900 rpm (in this sequence), and the ring electrode was kept at 1.4 V. During the measurement, oxygen was only passed over the surface of the electrolyte. Tafel plots have been calculated by the Levich approach. The relative formation of hydrogen peroxide was determined with a collection efficiency of 0.22.

For measuring the stability of IAL catalysts (“Stability in accelerated stress test” section), experiments were performed in a three-electrode arrangement with a glassy carbon counter electrode, an Ag/AgCl reference electrode and a glassy carbon disc with the catalyst as working electrode. Here, the catalyst

**Fig. 2** Cyclic voltammetry (a), Tafel plots (b) and hydrogen peroxide formation (c) of IAL catalysts and IAL intermediates in 0.5 M H<sub>2</sub>SO<sub>4</sub> measured with a catalyst loading of 0.13 mg cm<sup>-2</sup>. Tafel plots were obtained by using currents corrected for mass transport using the Levich approach; details are given in the “Experimental part” section



loading was 0.5 mg cm<sup>-2</sup> and the Nafion to catalyst ratio 1:4. Previous to the stability evaluation under two accelerated stress test (AST) conditions (see Table 1), cyclic voltammograms were obtained with a sweep rate of 100 mV s<sup>-1</sup>. These two protocols were utilized to mimic the performance of the catalyst under run conditions (AST\_Run) and during start-up and shutdown conditions (AST\_SSC).

The ORR activity was determined from RDE obtained with 1600 rpm and a sweep rate of 10 mV s<sup>-1</sup> in oxygen-saturated 0.5 M H<sub>2</sub>SO<sub>4</sub>. The evaluation of the activity decay includes similar measurements of ORR activity after a specified number of cycles in AST and the performance of an additional cyclic voltammogram in nitrogen-saturated electrolyte with 100 mV s<sup>-1</sup>. This is required to follow changes in the capacity and redox behaviour of the catalysts due to the AST protocol. For the evaluation of the activity decay, either the time of cycling, number of cycles or relative change of potential can be used. This  $\Delta U$  value is given as a product of the potential range and the number of half-cycles. Potentials are always given in reference to the standard hydrogen electrode (RHE).

**Möbbsbauer spectroscopy** Möbbsbauer measurements were made to characterize the iron compounds within each IAL catalyst. The spectra were recorded at RT with a CMCA-550 (Wissel) equipped with a constant electronic drive system with triangular reference wave form (Halder Electronics). A Co-57/Rh source was used, and velocity scale and isomer shift  $\delta_{\text{iso}}$  were calibrated with natural iron ( $\alpha$ -Fe foil, 25  $\mu$ m thick, 99.99 % purity). Assignment of iron species was made by a comparison of the Möbbsbauer parameters to literature data.

**X-ray diffraction** For the identification of crystalline phases, XRD measurements of IAL intermediates and IAL catalysts were carried out employing a Bruker diffractometer D8 Advance in Bragg-Brentano  $\Theta$ -2 $\Theta$  geometry using Cu K $\alpha$  radiation ( $\lambda$ =1.54 Å) and a silicon disc as sample holder. Samples were rotated during the measurements. Spectra were recorded in a range of 15°<2 $\Theta$ <60°. The measured diffractograms were analyzed using the database of the Joint Committee on Powder Diffraction Standards (JCPDS).

**Table 1** Summary of the conditions for the AST\_Run and AST\_SSC protocol

	AST_Run	AST_SSC
Conditions	0.0–1.0 V, 300 mV s <sup>-1</sup>	0.0–1.5 V, 500 mV s <sup>-1</sup>
Initial activity	0 cycles ( $t$ =0.0 h, $\Delta U$ =0 V)	0 cycles ( $t$ =0.0 h, $\Delta U$ =0 V)
Evaluation of activity decay	270 cycles ( $t$ =0.5 h, $\Delta U$ =540 V) 810 cycles ( $t$ =1.5 h, $\Delta U$ =1620 V) 2430 cycles ( $t$ =4.5 h, $\Delta U$ =4860 V)	500 cycles ( $t$ =0.28 h, $\Delta U$ =500 V) 2000 cycles ( $t$ =1.11 h, $\Delta U$ =2000 V) 5000 cycles ( $t$ =2.78 h, $\Delta U$ =5000 V)

Evaluation of the activity decay always includes the measurement of a cyclic voltammogram and a RDE



**Raman spectroscopy** For the micro-Raman measurements, the catalysts were dispersed in Milli-Q water, and then, a drop was placed on a cleaned glass coverslip on an Olympus IX71 microscope, and the samples were left to dry before measuring. For the measurement of degraded catalysts, after AST\_SSC, the catalyst layer was scraped off the glassy carbon (GC) tip and 100  $\mu\text{L}$  of Milli-Q water was added to re-disperse the catalyst following the same procedure as given above. A 514-nm CW Argon Ion laser (CVI Melles Griot 35 MAP431-200) was aligned into the microscope. Two narrow-band-pass filters centred at 510 and 514 nm (Semrock FF02-510/20-25 and FF01-514/3-25) were used to spectrally clean the laser source. The laser light was reflected in the microscope on a 70/30 beam splitter (XF122 from Omega Filters) towards a  $\times 100$  1.3 NA immersion oil objective (Olympus U plan FL N) that focused the laser on the sample and collected the Raman signal. The power of the laser focused into a diffraction-limited spot at the sample was 17  $\mu\text{W}$  (ca. 34  $\text{kW cm}^{-2}$ ). Two 514-nm-long pass filters (Semrock LP02-514RE-25 and LP02-514RU-25) were used to block the 514-nm laser light in the detection path. The Raman spectrum was recorded by using a PI Acton SpectraPro SP-2356 polychromator (600  $\text{g mm}^{-1}$  blazed at 500 nm) and a PI Acton SPEC-10:100B/LN eXcelon Spectroscopy System with a back-illuminated CCD chip (1340  $\times$  100 pixels). X-axis calibration of the spectra was performed after the measurements using a toluene Raman spectrum and a Neon pencil calibration lamp (ORIEL instruments, 6032 neon lamp). For better comparison of the spectra, the intensity was normalized to the D-band maximum after background subtraction with a linear function ( $y=ax+b$ ). Spikes in the spectrum due to cosmic rays were removed manually.

In addition, for IAL intermediates, Pyrolysis Products 2 and IAL catalysts, the iron contents were determined by neutron activation analysis (NAA) at the Helmholtz Center in Berlin by D. Alber and her co-workers; these values are summarized in Table 2 and compared to the standard catalysts and the calculated iron contents in the precursor and Pyrolysis Products 1.

## Results and discussion

### Characterization of the intermediate acid leaching catalysts

In the first step, the electrochemical performance of the IAL intermediates and IAL catalysts is compared. In Fig. 2, typical cyclo-voltammograms, the Tafel plots and the relative content of hydrogen peroxide during RRDE experiment are compared for the differently prepared samples. In general, the sulphur-free IAL preparation leads to a higher double-layer capacity and better electronic conductivity in comparison to the IAL preparation with sulphur addition.

The reduced electronic conductivity of the IAL intermediate (+S) and the IAL catalyst (+S) leads to a tilted shape of the CV curves. In contrast, the IAL catalyst (−S) depicts a nearly ideal electronic behaviour. A redox peak at 0.65 V can be assigned to the  $\text{Fe}^{3+}/\text{Fe}^{23+}$  or quinone/hydroquinone [25, 41]. For non-pyrolyzed macrocycles, the potential at which this redox peak appears correlates with the catalytic performance of the macrocycles [42–44]. However, the appearance of the redox peak is no precondition for high ORR, since both IAL catalysts reach a similar high activity (Fig. 2b), but only for the sulphur-free IAL catalyst, a redox peak is observed in the CV. The kinetic current densities of both IAL catalysts are a factor of four higher in comparison to the IAL intermediates. Also, the selectivity is improved by continuing the heat treatment process to 800 °C with subsequent acid leaching. In general, it is enhanced by 33 %. This factor is similar for both preparation strategies, i.e. with or without sulphur. Interestingly, 33 % equals the removal of 33 % of iron for the same catalysts, as compared to Table 2. This might be an indication that most of the hydrogen peroxide formation is not related to the most active  $\text{FeN}_4$  sites but to inorganic iron species (magnetite, iron carbide) that are capable of an indirect reduction of oxygen to hydrogen peroxide but reveal a limited stability in acidic conditions [45, 46]. In an alternative explanation mode, one could assume that the ORR mechanism on the  $\text{FeN}_4$  sites is changed going from 500 to 800 °C. However, our own results for carbon-supported iron-porphyrin-based

**Table 2** Concentration of iron (wt%) in the different samples investigated in this work

	In Prec. <sup>a</sup>	Standard	Pyrolysis Prod. 1 <sup>b</sup>	IAL intermediate	Pyrolysis Prod. 2	IAL catalyst
Without sulphur	26.8	8.9	57.6	24.6	32.0	15.8
With sulphur	25.6	3.0	56.9	8.6	11.7	5.4

<sup>a</sup> Values are calculated from the precursor composition

<sup>b</sup> Estimated values are *calculated* from the precursor composition and the relative mass remaining after a heat treatment to 500 °C (as determined from thermogravimetric measurements). Due to a subsequent oxidation of the iron after contact to air, the real iron content might be a little smaller. For example, for the standard catalyst based on similar estimation, one would obtain an iron content of 77.6 wt% while the as-measured content by NAA was 65.6 wt% due to subsequent oxidation

catalysts illustrated that, basically, the turnover frequency is changed by the variation of the pyrolysis temperature [6]. Measurements on hydrogen peroxide formation gave similar values for catalysts prepared at  $\geq 600$  °C (500 °C was not investigated) [47]. Hence, we assume that the change in selectivity observed in this work is more likely due to the removal of inorganic iron species. Indeed, our structural characterization by Mößbauer spectroscopy and X-ray diffraction confirms the presence of these particles predominantly in the IAL intermediates.

It should be noted that the catalyst loading for the selectivity measurements was relatively low in this work. For several non-precious metal catalysts, it was shown that the achieved hydrogen peroxide formation strongly depended on the catalyst loading [28, 48–50]. Compared to these NPMC measured with similar loadings, our values are either similar or smaller.

Figure 3 presents the Mößbauer spectra of the IAL intermediates and the IAL catalysts. Table 3 summarizes the average Mößbauer parameters and the assignment to iron species (please note: we did not perform Mößbauer spectroscopy on the Pyrolysis Products 1 (i.e. after heat treatment to 500 °C *without* acid leaching). Due to the chosen precursor composition and the decomposition processes taking place up to 500 °C, these Pyrolysis Products 1 contain nearly about 60 wt% iron (compare Table 2) due to the large quantity of iron oxalate in the precursor mixture. Hence, it can be assumed that its decomposition products will also dominate the Mößbauer spectra. Also, in HT-XRD, basically, the crystallographic changes related to the iron oxalate, but not for the porphyrin, were observable [29]. In that work, basically, wuestite and magnetite were detected in situ at 500 °C.)

In the first step, the spectra of the sulphur-free IAL approach are discussed. The intermediate is dominated by two sextets. Sextets 1A and 1B are both related to iron sites in the

magnetite structure [51]. The higher magnetic field is related to the ferric iron in a tetrahedral environment (site 1A), with an isomer shift of  $\delta_{\text{iso}} = 0.31$  mm s<sup>-1</sup>. The iron in site 1B is in octahedral coordination with oxygen and hosts both Fe<sup>2+</sup> and Fe<sup>3+</sup> ions. Due to a fast hopping process, the subspectra of each ion cannot be resolved at RT. Consequently, the isomer shift value is an average between Fe<sup>3+</sup> high spin and Fe<sup>2+</sup> high spin ( $\delta_{\text{iso}} = 0.66$  mm s<sup>-1</sup>). The observation of the magnetite compound is not unexpected, as our HT-XRD showed that magnetite forms at about 500 °C [29]. Formed at high temperature, it is difficult to remove magnetite by acid leaching [52], which explains the presence of this species even after the IAL.

The doublets in this spectrum are both assigned to FeN<sub>4</sub> sites that differ in their local environments. The green doublet D1 is well known from several porphyrin-based catalysts [2, 3, 6, 8] and alternative preparation approaches [4, 7, 9, 12, 32]. In a previous work, it was identified as the ORR-active sites in Fe–N–C catalysts. It is a FeN<sub>4</sub> site with Fe<sup>2+</sup> in the low-spin state. The second doublet D2 has similar Mößbauer parameters as iron phthalocyanine (FePc). For carbon-supported FePc, Melendres found two Mößbauer doublets [53]: one with the typical signature of crystalline FePc (where the large quadrupole splitting is induced by the interaction of the metal centre with nitrogen atoms from the FePc molecules on top and below in axial direction) and a second one with Mößbauer parameters similar to our D1 site. Melendres interpreted the appearance of this doublet with the formation of a surface-attached Fe<sup>II</sup>N<sub>4</sub> site. The Mößbauer parameters are different to the crystalline FePc, as instead of the interaction with two nitrogen atoms (from the FePc molecules on top and below), these FePc molecules lie flat on the graphene sheets of the utilized carbon support.

**Fig. 3** Mößbauer spectra of the IAL intermediates (a, c) and IAL catalysts (b, d). Measurements were performed at RT with a calibration with respect to  $\alpha$ -Fe. The colour code is equal to Table 2, where the Mößbauer parameters and the assignment to iron species are summarized

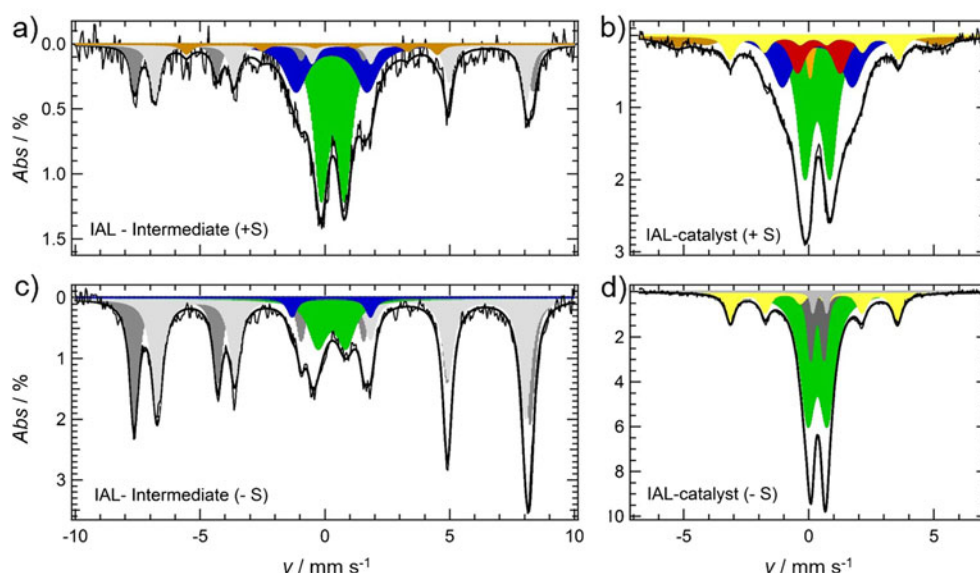


**Table 3** Summary of the average Mößbauer parameters and absorption areas of the IAL intermediates and IAL catalysts

	$\delta_{iso} /$ mm s <sup>-1</sup>	$\Delta E_Q /$ mm s <sup>-1</sup>	$H_0 /$ G	$fwhm /$ mm s <sup>-1</sup>	Area / %		Area / %		Assignment
					IAL-interm.		IAL-cat		
					(-S)	(+S)	(-S)	(+S)	
Sing	0.05	-	-	0.3 (f)	-	-	-	2.9	Nano-Iron
D 1	0.32	0.96	-	0.74	14.3	40.3	62.6	41.7	Fe <sup>2+</sup> N <sub>4</sub> , LS
D 2	0.30	2.83	-	1.02	3.0	20.1	-	22.8	Like FePc
D 3	0.40	1.71	-	0.70	-	-	-	11.4	Like [FePc] <sup>2-</sup>
D 4A	0.34	0.54	-	0.30	-	-	14.7	-	Nano-Fe <sub>x</sub> N or Nano- FeO
D 4B	0.43	0.55	-	0.20			3.0		
Sext 1A	0.31	0.01	493	0.41	38.4	15.3	-	-	Magnetite
Sext 1B	0.66	0.01	459	0.48	44.4	20.6			
Sext 2	-0.31	0.21	318	0.83	-	3.7	-	10.6	a-Fe
Sext 3	0.20	0.02	208	0.47	-	-	19.7	10.6	Iron carbide

The label (f) denotes fixed values during the fitting process. The colour code is similar to Fig. 3

Upon continuing the heat treatment (RT to 800 °C) with subsequent acid leaching, the Mößbauer signature of the corresponding IAL catalyst (-S) changes in comparison to its IAL intermediate. No magnetite is found anymore. This was, in general, also expected because also the standard catalyst (-S) does not contain any magnetite when prepared at 800 °C. Continuing the heat treatment to 800 °C, magnetite reacts further to iron carbide (sext 3) induced by the reducing environment provided by carbon. Besides the small iron carbide fraction, there are two doublets (D4A, B) that can be assigned to iron nitride or hematite nanoparticles [51]. That means that this catalyst contains exclusively the D1-related FeN<sub>4</sub> sites. Hence, this confirms our previous observation that only this particular site drives the ORR activity in porphyrin-based catalysts [6, 8, 54].

Let us now discuss the differences and similarities towards the catalysts prepared with sulphur. As expected, also the sulphur-containing IAL intermediate contains the ORR-active FeN<sub>4</sub> site assigned to D1, the D2 doublet (FePc) and significant contributions of magnetite (sext 1A and 1B). In addition, a small fraction of  $\alpha$ -Fe is found (sext 2 in the spectra). Also, the formation of alpha-iron is in accordance with our previous HT-XRD study [29].

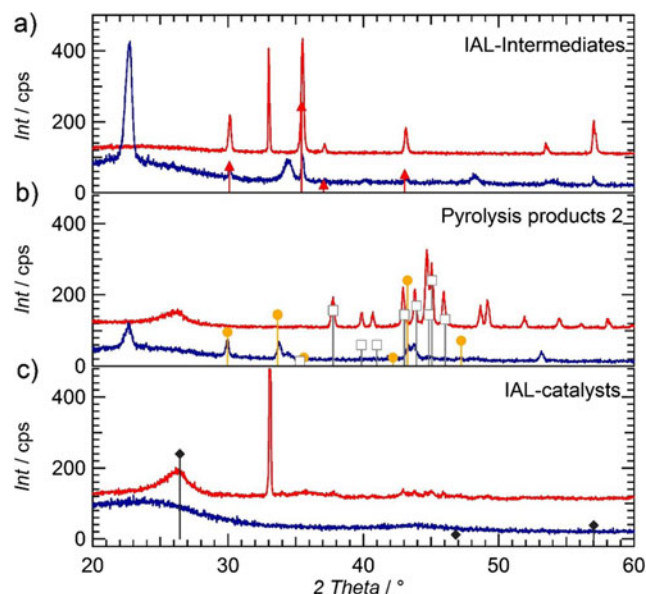
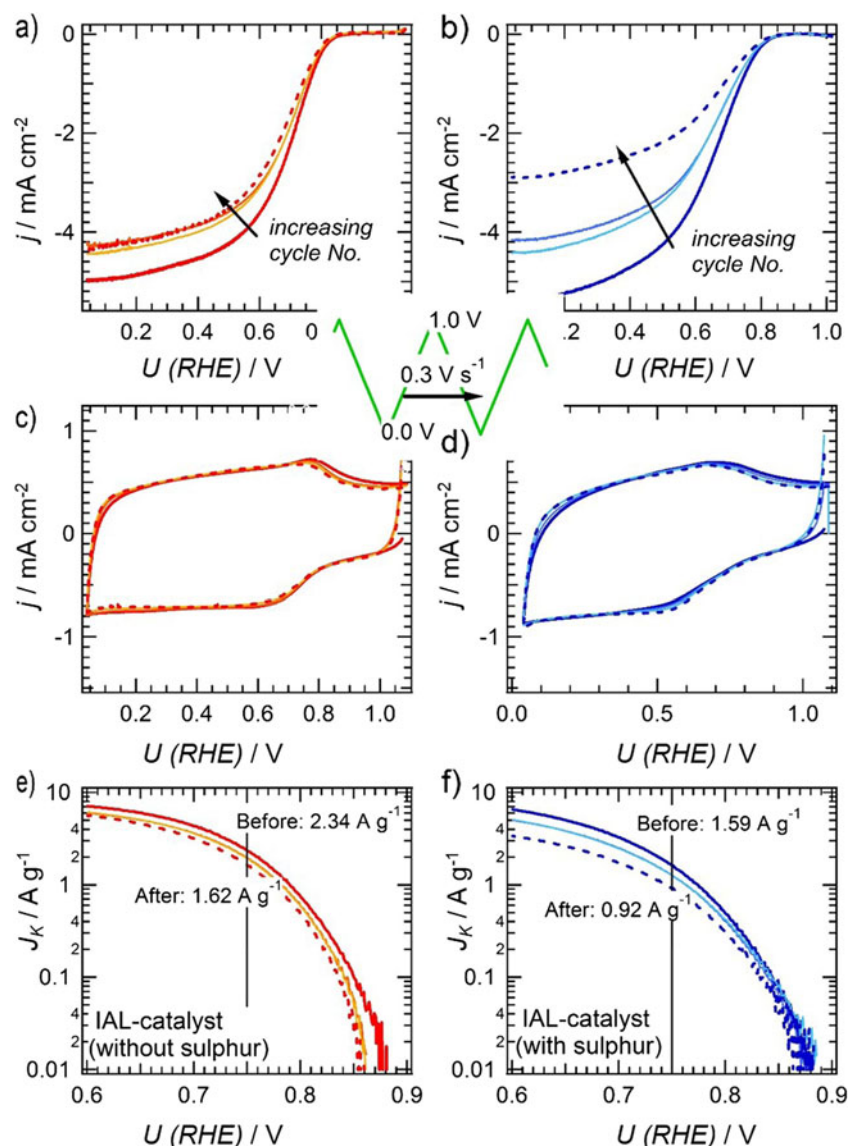


**Fig. 4** X-ray diffraction measurements of the IAL intermediates and IAL catalysts as well as the Pyrolysis Products 2. The JCPDS data of magnetite (triangles, 19-0629), iron carbide (squares, 23-1113), troilite (circles, JCPDS 11-0151) and graphite (diamond, JCPDS 8-0415) are given

**Fig. 5** Results of the AST\_Run measurements with respect to changes in RDE curves (a, b), cyclo-voltammograms (c, d) and Tafel plots (e, f) for the sulphur-free (left side) and sulphur-added (right side) IAL catalysts (—/— start, —/— 270, —/— 810, - - - - 2430 cycles)



If the heat treatment is continued to 800 °C with subsequent acid leaching (IAL catalyst), the Mößbauer spectrum resembles that of the standard catalyst prepared under sulphur addition. In this case, however, there are some small sextet contributions related to iron carbide and alpha-iron [51].

Due to the dominance of Mößbauer signals attributed to inorganic iron species, we did not determine the content of iron assigned to each species. This would require similar Debye-Waller factors of all components. Usually, inorganic iron species reveal a higher recoil-free fraction (expressed in the Debye-Waller factor) in comparison to FeN<sub>4</sub> sites. However, with respect to Goellner et al. [10], we would like to point out that although it is dominating the Mößbauer spectra, the overall content of iron in these inorganic species might not be as pronounced. This is also supported by the X-ray diffractograms given in Fig. 4.

Our X-ray diffractograms (Fig. 4a–c) confirm the presence of crystalline iron phases in the IAL intermediates and Pyrolysis Products 2. Some diffractograms show the reflex from the Si substrate at  $2\theta=33^\circ$ . After the final heat treatment plus acid leaching, only the sulphur-free IAL catalyst depicts some very low-pronounced reflexes assigned to iron carbide (Fig. 4c). The final IAL catalyst (+S) exhibits an X-ray amorphous behaviour. Hence, while the Mößbauer spectra clearly show the presence of sextets, these were not identified by XRD. Obviously, the content of these Fe<sub>3</sub>C particles is low so that they do not contribute significantly to the diffractogram. Furthermore, while there is a broad reflex at  $2\theta=26^\circ$  for the IAL catalyst (–S), this is even broadened for the IAL catalyst (+S) and shifted to smaller  $2\theta$  values, indicating a larger distance of the graphene planes due to smaller van der Waals interaction. For the sulphur-containing IAL



intermediate and Pyrolysis Product 2, there is a well-pronounced reflex at  $2\Theta=23^\circ$  that we were not able to assign.

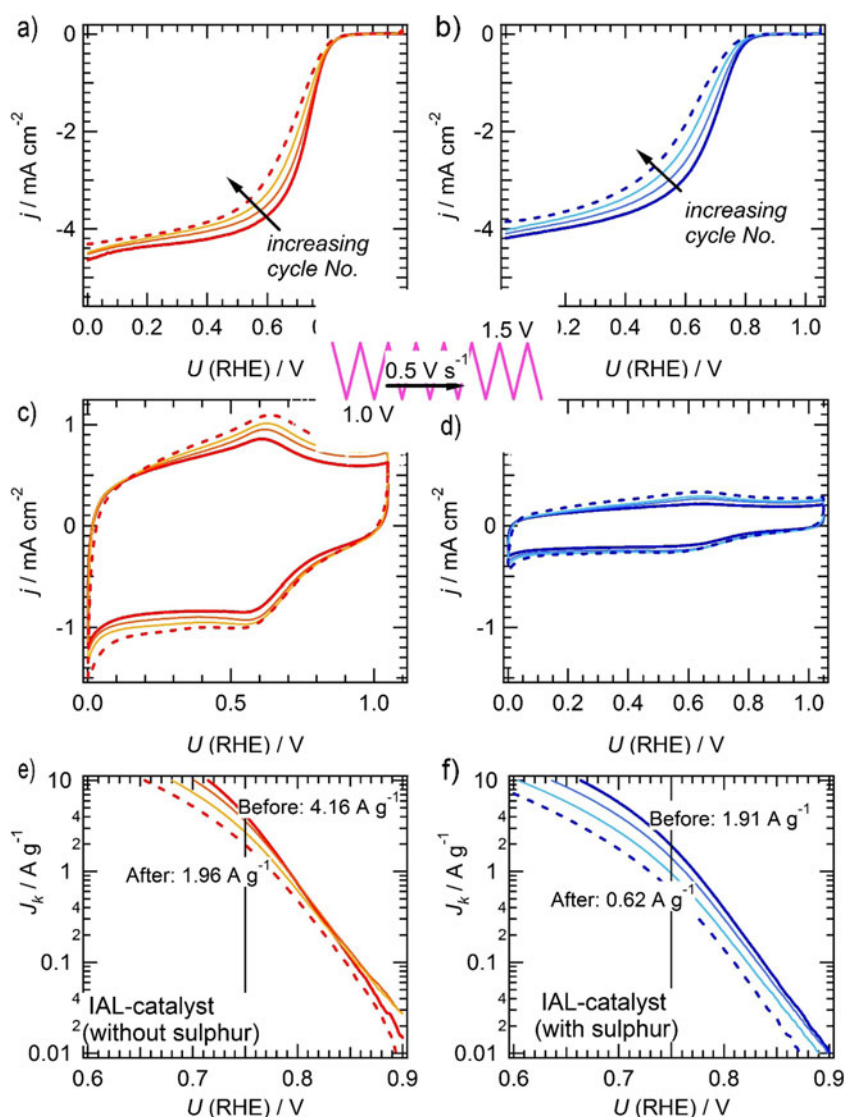
### Stability in accelerated stress tests

In the next step, we evaluated the stability of the IAL catalysts. Two different test protocols were applied. The first one mimics the standard operation conditions in PEM-FC, referred to as *AST\_Run*. The second protocol is applied to evaluate the stability of the catalysts under start-up and shutdown conditions of PEM-FC. This AST protocol will be referred to as *AST\_SSC* (start-stop conditions). For both AST protocols, the catalyst's performances are tested at the beginning and some specific cycle numbers at the end of the AST protocol by RDE measurements (1600 rpm) (compare Table 1 in the “Experimental part” section). In Figs. 5 and 6, the results of the *AST\_Run* and *AST\_SSC* measurements are summarized,

respectively. Figures 5a, b and 6a, b display the RDE measurements, Figs. 5c, d and 6c, d the cyclo-voltammograms and Figs. 5e, f and 6e, f the Tafel plots after specific cycle numbers as given in the figure captions. The results of both AST protocols are directly compared in Fig. 7 as a function of  $\Delta U$  (see “Experimental part” section) which turns out to be a better parameter for the comparison than cycle number or time of measurement.

Simulating the potential changes during standard FC operation (Fig. 5) leads to a fast initial decay of ORR activity by 15–20 % within the first 30 min of testing ( $\Delta U=540$  V) for both IAL catalysts. In the subsequent cycling, the decay is more pronounced for the IAL catalyst prepared under sulphur addition (down to 60 % of initial activity) compared to the sulphur-free one (down to 70 % of initial activity). For the sulphur-free IAL catalyst, the diffusion limiting current is only changed within the first 30 min of operation and stays constant afterwards. In contrast, the current plateau that is reached for

**Fig. 6** Results of the *AST\_SSC* measurements with respect to changes in RDE curves (a, b), cyclo-voltammograms (c, d) and Tafel plots (e, f) for the sulphur-free (left side) and sulphur-added (right side) IAL catalysts (—/— start, —/— 500, —/— 2000, - - - - 5000 cycles)



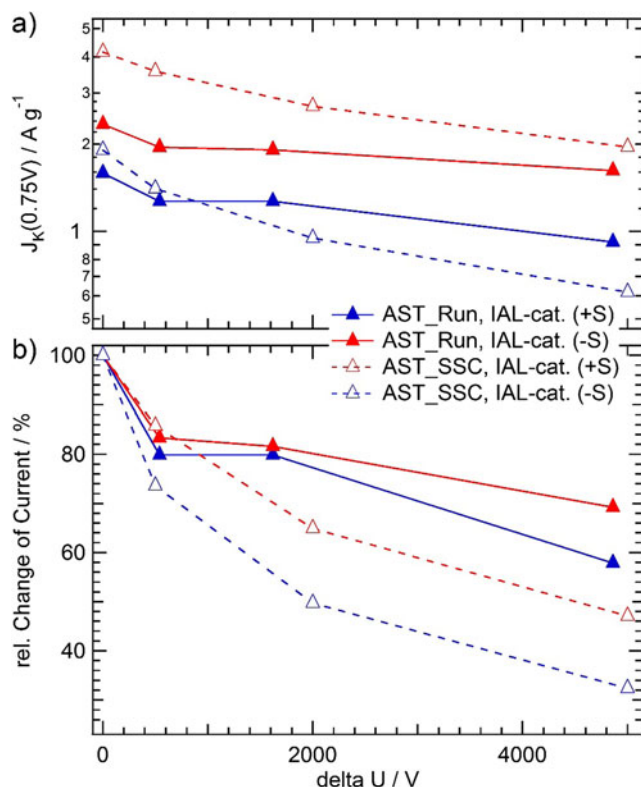


**Fig. 7** **a** Change of the mass-related kinetic current density at 0.75 V and **b** relative change of kinetic current density as a function of  $\Delta U$  applied to the catalysts during the two different AST protocols (compare Table 1)

the sulphur-added IAL catalyst is decreased by a factor of two from the initial RDE curve to the final one. Based on the relation that the diffusion limiting current density  $j_{Diff} \sim n_e$ , the number of transferred electrons, this could indicate a change in selectivity by a factor of 2—in other words, changing from a predominating four-electron reduction to a two-electron reduction to hydrogen peroxide. Another possible explanation would be a partial removal of the catalyst layer from the RDE. In this case, however, one would also expect a decrease in the capacity current in Fig. 5d which is not observed. In addition, the cyclic voltammograms can be used to identify changes in the surface structure of the carbon. Applying this AST\_Run protocol does not lead to a significant change for any of both catalysts. This is also expected, as usually up to 1.1 V, the carbon oxidation is kinetically hindered if no particles are present to accelerate this reaction [35, 55].

How do these results compare to that obtained for the AST\_SSC protocol, shown in Fig. 6? Interestingly, for both IAL catalysts, the changes in the diffusion limiting current densities are not as pronounced as for the AST\_Run protocol. With increasing cycle number, the Tafel slope (Butler-Volmer behaviour) decreases. The reason for this behaviour might be a decrease of either the exchange current density  $j_0$  and/or the transfer coefficient  $\alpha$ . The Tafel plots in Fig. 6e, f indicate

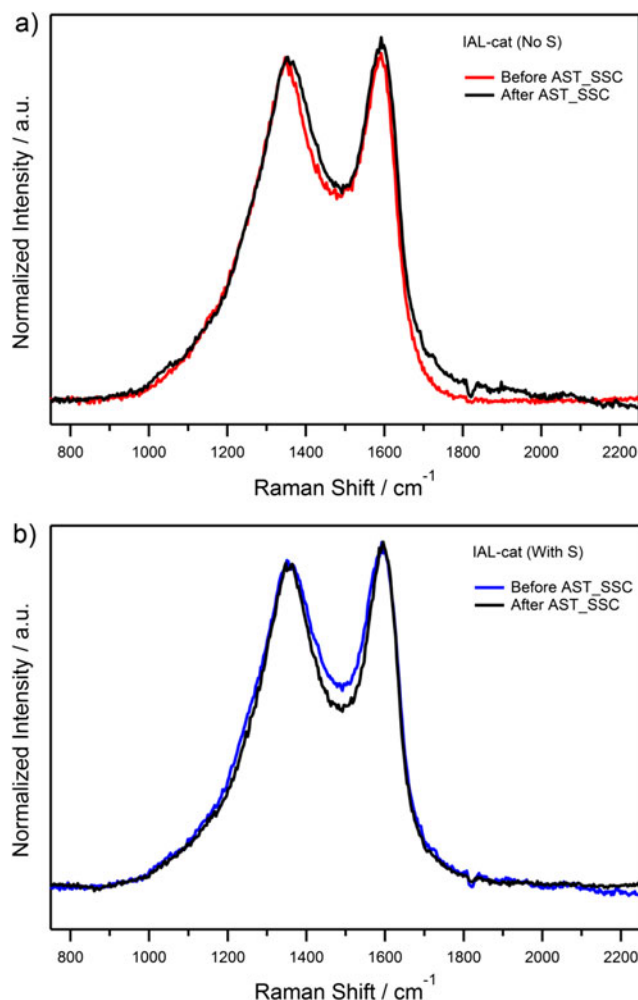


**Fig. 8** Raman spectra of the IAL catalysts before and after AST\_SSC for the sulphur-free (**a**) and sulphur-added (**b**) catalyst. To obtain the spectra, the individual spectra of four different areas (catalyst flakes) were background subtracted, added and normalized to the intensity of the D band. The individual spectra are shown in the supporting information

both. In addition, the applied high potential range leads to the formation of surface groups as can be noted from the increase in capacity in Fig. 6c, d. For AST\_SSC, the decrease in current density over time is most pronounced for the sulphur-added IAL catalyst. Five thousand cycles are sufficient to decrease the ORR activity to about 30 % of its initial value.

For an easy comparison of ORR activity and decrease over  $\Delta U$ , the mass-related kinetic current densities at 0.75 V are given in Fig. 7a, whereas the relative changes in current densities at 0.75 V are compared in Fig. 7b.

It is interesting to note that the sulphur-free IAL catalyst performs more stable in comparison to the sulphur-added IAL catalyst under both conditions. The sulphur-added IAL catalyst decays much faster in the high-potential window that mimics the start-up and shutdown conditions of FC operation (AST\_SSC). The reason for this might be a lower definition of the carbon as expressed by a less pronounced carbon reflex in

the X-ray diffractograms (Fig. 4c). In order to verify this in more details, we performed micro-Raman spectroscopy on the as-prepared catalysts and after AST\_SSC. The comparison of the averaged and normalized spectra is given in Fig. 8.

The spectra are typical for highly amorphous carbons with a nearly equal ratio of G band (at  $1575\text{ cm}^{-1}$ ) to D band (at  $1350\text{ cm}^{-1}$ ) and a large amorphous contribution expressed in the intensity between D band and G band ( $D_3$  band at ca.  $1500\text{ cm}^{-1}$ ) [20, 56]. Besides these bands, a small shoulder at  $1750\text{ cm}^{-1}$  is seen for the sulphur-free IAL catalyst after AST\_SSC. A similar shoulder was found for Vulcan and Pt/Vulcan catalyst after oxidizing treatment under the same AST conditions [35]. In relation to the paper by Hiramitsu et al., we assign this peak to the formation of carbonyl groups on the surface of the carbon [57]. Locally resolved Raman spectra of single flakes (see supporting information) reveal that small changes of the catalyst before and after AST\_SSC can be due to inhomogeneity and have to be interpreted with care. On the other hand, also the electrochemical measurements give an integral result of a large number of individual flakes. Interestingly, based on four points, it seems that the pristine sulphur-free IAL catalyst is less homogeneous than the sulphur-added IAL catalyst. In none of the spectra, a significant change in the D band to G band ratio is observed upon AST\_SSC. In contrast, a formation of the shoulder at  $1750\text{ cm}^{-1}$  and a decrease of the  $D_3$  band are observed for the sulphur-free and sulphur-added IAL catalyst, respectively, in the integral measurements shown in Fig. 8. It can therefore be postulated that the observed performance degradation of the catalysts is not dominated by the same degradation scheme for sulphur-free and sulphur-added IAL-catalysts. More detailed studies will be required in order to work out the dominating degradation modes.

## Conclusion

In conclusion, our results illustrate that the utilization of an IAL can be used to prevent active site destruction during catalyst formation, as similar high ORR activity can be gained as previously achieved by the addition of sulphur. In its current form, both IAL catalysts still contain fractions of inorganic iron species. However, we believe that with a further optimization of the preparation process, these fractions can be eliminated. In addition, it is expected that the activity can be enhanced by some subsequent heat treatments in either inert or reactive gas atmosphere [2, 8, 9, 25, 54]. Our AST stability results demonstrate a significant smaller activity loss for the sulphur-free IAL catalyst compared to the sulphur-added one under both operation conditions.

**Acknowledgments** This work was supported by the European Fund for Regional Development (EFRE) at BTU Cottbus under the Project No. 1307513, by the German Research Foundation (DFG) within the initiative of the Graduate School of Excellence Energy Science and Engineering (ESE, GSC 1070) at TU Darmstadt and by the Danish Innovation Fund (“non-precious” project). In addition, we would like to thank D. Alber and her co-workers for the performance of neutron activation analysis of our samples.

## References

1. de Frank Bruijn A, Janssen GJM (2013) PEM fuel cell materials: costs, performance and durability. Encyclopedia of Sustainable Science and Technology. Springer NY
2. Koslowski UI, Abs-Wurmbach I, Fiechter S, Bogdanoff P (2008) Nature of the catalytic centres of porphyrin based electrocatalysts for the ORR—a correlation of kinetic current density with the site density of Fe-N<sub>4</sub> centres. *J Phys Chem C* 112(39):15356–15366
3. Tributsch H, Koslowski U, Dorbandt I (2008) Experimental and theoretical modeling of Fe-, Co-, Cu-, Mn-based electrocatalysts for oxygen reduction. *Electrochim Acta* 53(5):2198–2209
4. Ferrandon M, Kropf AJ, Myers DJ, Artyushkova K, Kramm U, Bogdanoff P, Wu G, Johnston CM, Zelenay P (2012) Multitechnique characterization of a polyaniline-iron-carbon oxygen reduction catalyst. *J Phys Chem C* 116:16001–16013
5. Herranz J, Jaouen F, Lefevre M, Kramm UI, Proietti E, Dodelet J-P, Bogdanoff P, Fiechter S, Abs-Wurmbach I, Bertrand P, Arruda T, Mukerjee S (2011) Unveiling N-protonation and anion-binding effects on Fe/N/C-catalysts for O<sub>2</sub> reduction in PEM fuel cells. *J Phys Chem C* 115:16087–16097
6. Kramm UI, Abs-Wurmbach I, Herrmann-Geppert I, Radnik J, Fiechter S, Bogdanoff P (2011) Influence of the electron-density of FeN<sub>4</sub>-centers towards the catalytic activity of pyrolysed FeTMPPCl-based ORR-electrocatalysts. *J Electrochem Soc* 158(1):B69–B78
7. Kramm UI, Herranz J, Larouche N, Arruda TM, Lefèvre M, Jaouen F, Bogdanoff P, Fiechter S, Abs-Wurmbach I, Mukerjee S, Dodelet J-P (2012) Structure of the catalytic sites in Fe/N/C-catalysts for O<sub>2</sub>-reduction in PEM fuel cells. *Phys Chem Chem Phys* 14:11673–11688
8. Kramm UI, Herrmann-Geppert I, Bogdanoff P, Fiechter S (2011) Effect of an ammonia treatment on structure, composition and ORR activity of Fe-N-C catalysts. *J Phys Chem C* 115:23417–23427
9. Kramm UI, Lefèvre M, Larouche N, Schmeisser D, Dodelet J-P (2014) Correlations between mass activity and physicochemical properties of Fe/N/C catalysts for the ORR in PEM fuel cell via <sup>57</sup>Fe Mössbauer spectroscopy and other techniques. *J Am Chem Soc* 136(3):978–985
10. Goellner V, Baldizzone C, Schuppert A, Sougrati MT, Mayrhofer K, Jaouen F (2014) Degradation of Fe/N/C catalysts upon high polarization in acid medium. *Phys Chem Chem Phys* 16:18454–18462
11. Morozan A, Sougrati MT, Goellner V, Jones D, Stievano L, Jaouen F (2014) Effect of furfuryl alcohol on metal organic framework-based Fe/N/C electrocatalysts for polymer electrolyte membrane fuel cells. *Electrochim Acta* 119:192–205
12. Tian J, Morozan A, Sougrati MT, Lefèvre M, Chenitz R, Dodelet J-P, Jones D, Jaouen F (2013) Optimized synthesis of Fe/N/C cathode catalysts for PEM fuel cells: a matter of iron–ligand coordination strength. *Angew Chem Int Ed* 52(27):6867–6870
13. Maruyama J, Abe I (2007) Fuel cell cathode catalyst with heme-like structure formed from nitrogen of glycine and iron. *J Electrochem Soc* 154(3):B297–B304



14. Maruyama J, Okamura J, Miyazaki K, Uchimoto Y, Abe I (2008) Hemoglobin pyropolymer used as a precursor of a noble-metal-free fuel cell cathode catalyst. *J Phys Chem C* 112(7):2784–2790
15. Maruyama J, Yamamoto M, Hasegawa T, Iwasaki S, Siroma Z, Mineshige A (2013) Carbonaceous thin film coated on nanoparticle as fuel cell catalyst formed by one-pot hybrid physical–chemical vapor deposition of iron phthalocyanine. *Electrochim Acta* 90:366–374
16. Herranz J, Lefevre M, Dodelet J-P (2009) Metal-precursor adsorption effects on Fe-based catalysts for oxygen reduction in PEM fuel cells. *J Electrochem Soc* 156(5):B593–B601
17. Jaouen F, Lefevre M, Dodelet J-P, Cai M (2006) Heat-treated Fe/N/C catalysts for O<sub>2</sub> electroreduction: are active sites hosted in micropores? *J Phys Chem B* 110(11):5553–5558
18. Szakacs CE, Lefevre M, Kramm UI, Dodelet J-P, Vidal F (2014) A density functional theory study of catalytic sites for oxygen reduction in Fe/N/C catalysts used in H<sub>2</sub>/O<sub>2</sub> fuel cells. *Phys Chem Chem Phys* 16:13654–13661
19. Herrmann I, Kramm UI, Fiechter S, Bogdanoff P (2009) Oxalate supported pyrolysis of CoTMPP as electrocatalysts for the oxygen reduction reaction. *Electrochim Acta* 54:4275–4287
20. Herrmann I, Kramm UI, Fiechter S, Brüser V, Kersten H, Bogdanoff P (2010) Comparative study of the carbonisation of CoTMPP by low temperature plasma and by heat treatment. *Plasma Process Polym* 7(6):515–526
21. Lefevre M, Proietti E, Jaouen F, Dodelet J-P (2009) Iron-based catalysts with improved oxygen reduction activity in polymer electrolyte fuel cells. *Science* 324:71–74
22. Proietti E, Jaouen F, Lefevre M, Larouche N, Tian J, Herranz J, Dodelet J-P (2011) Iron-based cathode catalyst with enhanced power density in polymer electrolyte membrane fuel cells. *Nat Commun* 2:416
23. Zhao D, Shui J-L, Grabstanowicz LR, Chen C, Commet SM, Xu T, Lu J, Liu D-J (2014) Highly efficient Non-precious metal electrocatalysts prepared from one-pot synthesized zeolitic imidazolate frameworks. *Adv Mater* 26(7):1093–1097
24. Wu G, More KL, Johnston CM, Zelenay P (2011) High-performance electrocatalysts for oxygen reduction derived from polyaniline, iron, and cobalt. *Science* 332:443–447
25. Jaouen F, Herranz J, Lefevre M, Dodelet J-P, Kramm UI, Herrmann I, Bogdanoff P, Maruyama J, Nagaoka T, Garsuch A, Dahn JR, Olson TS, Pylypenko S, Atanassov P, Ustinov EA (2009) A cross-laboratory experimental review of non-noble-metal catalysts for oxygen electro-reduction. *Appl Mater Interfaces* 1:1623–1639
26. Bogdanoff P, Herrmann I, Hilgendorff M, Dorbandt I, Fiechter S, Tributsch H (2004) Probing structural effects of pyrolysed CoTMPP-based electrocatalysts for oxygen reduction via new preparation strategies. *J New Mat Electrochem Systems* 7:85–92
27. Shui J-L, Chen C, Grabstanowicz L, Zhao D, Liu D-J (2015) Highly efficient nonprecious metal catalyst prepared with metal-organic framework in a continuous carbon nanofibrous network. *Proc Natl Acad Sci U S A* 112(34):10629–10634
28. Herrmann I, Kramm UI, Radnik J, Bogdanoff P, Fiechter S (2009) Influence of Sulphur on the pyrolysis of CoTMPP as electrocatalyst for the oxygen reduction reaction. *J Electrochem Soc* 156(10):B1283–B1292
29. Kramm UI, Herrmann-Geppert I, Fiechter S, Zehl G, Zizak I, Dorbandt I, Schmeißer D, Bogdanoff P (2014) Effect of iron-carbide formation on the number of active sites in Fe–N–C catalysts for the oxygen reduction reaction in acidic media. *J Mater Chem A* 2(8):2663–2670
30. Paddison SJ, Gasteiger HA (2013) PEM fuel cell materials, materials and design development challenges. *Encyclopedia of Sustainable Science and Technology*. Springer NY
31. Kramm UI, Herrmann I, Fiechter S, Zehl G, Zizak I, Abs-Wurnbach I, Radnik J, Dorbandt I, Bogdanoff P (2009) On the influence of sulphur on the pyrolysis process of FeTMPP-Cl-based electro-catalysts with respect to oxygen reduction reaction (ORR) in acidic media. *ECS Trans* 25(1):659–670
32. Kramm UI, Lefevre M, Bogdanoff P, Schmeißer D, Dodelet J-P (2014) Analyzing structural changes of Fe–N–C cathode catalysts in PEM fuel cell by Mößbauer spectroscopy of complete membrane electrode assemblies. *J Phys Chem Lett* 5:3750–3756
33. Hartl K, Hanzlik M, Arenz M (2011) IL-TEM investigations on the degradation mechanism of Pt/C electrocatalysts with different carbon supports. *Energy Environ Sci* 4(1):234–238
34. Speder J, Zana A, Spanos I, Kirkensgaard JJK, Mortensen K, Hanzlik M, Arenz M (2014) Comparative degradation study of carbon supported proton exchange membrane fuel cell electrocatalysts—the influence of the platinum to carbon ratio on the degradation rate. *J Power Sources* 261:14–22
35. Zana A, Speder J, Reeler NEA, Vosch T, Arenz M (2013) Investigating the corrosion of high surface area carbons during start/stop fuel cell conditions: a Raman study. *Electrochim Acta* 114:455–461
36. Zana A, Speder J, Roefzaad M, Altmann L, Bäumer M, Arenz M (2013) Probing degradation by IL-TEM: the influence of stress test conditions on the degradation mechanism. *J Electrochem Soc* 160(6):F608–F615
37. Reiser CA, Bregoli L, Patterson TW, Yi JS, Yang JD, Perry ML, Jarvi TD (2005) A reverse-current decay mechanism for fuel cells. *Electrochem Solid-State Lett* 8(6):A273–A276
38. Patterson TW, Darling RM (2006) Damage to the cathode catalyst of a PEM fuel cell caused by localized fuel starvation. *Electrochem Solid-State Lett* 9(4):A183–A185
39. Ferrandon M, Wang X, Kropf AJ, Myers DJ, Wu G, Johnston CM, Zelenay P (2013) Stability of iron species in heat-treated polyaniline–iron–carbon polymer electrolyte fuel cell cathode catalysts. *Electrochim Acta* 110:282–291
40. Ohma A, Shinohara K, Iiyama A, Yoshida T, Daimaru A (2011) Membrane and catalyst performance targets for automotive fuel cells by FCCJ membrane, catalyst, MEA WG. *ECS Trans* 41(1):775–784
41. Gojkovic SL, Gupta S, Savinell RF (1998) Heat-treated iron(III) tetramethoxyphenyl porphyrin chloride supported on high area carbon as an electrocatalyst for oxygen reduction part I: characterization of the electrocatalyst. *J Electrochem Soc* 145(10):3493–3499
42. Zagal JH, Páez M, Sturm J, Ureta-Zañartu S (1984) Electroreduction of oxygen on mixtures of phthalocyanines co-adsorbed on a graphite electrode. *J Electroanal Chem* 181:295–300
43. Zagal JH, Páez M, Silva JF (2006) Fundamental aspects on the catalytic activity of metallomacrocyclics for the electrochemical reduction of O<sub>2</sub>. In: Zagal JH, Bedioui F, Dodelet J-P (eds) *N<sub>4</sub>-macrocyclic metal complexes*. Springer, New York, pp 41–82
44. Zagal JH, Ponce I, Baez D, Venegas R, Pavez J, Paez M, Gulppi M (2012) A possible interpretation for the high catalytic activity of heat-treated non-precious metal Nx/C catalysts for O<sub>2</sub> reduction in terms of their formal potentials. *Electrochem Solid-State Lett* 15(6):B90–B92
45. Wu Z-S, Yang S, Sun Y, Parvez K, Feng X, Müllen K (2012) 3D nitrogen-doped graphene aerogel-supported Fe<sub>3</sub>O<sub>4</sub> nanoparticles as efficient electrocatalysts for the oxygen reduction reaction. *J Am Chem Soc* 134:9082–9085
46. Gojkovic SL, Zecevic SK, Drazic DM (1994) Oxygen reduction on iron—part VI. Processes in alkaline solution. *Electrochim Acta* 39(7):975–982
47. Kramm UI (2009) Die strukturelle Einbindung des Eisens in Eisenporphyrin-Elektrokatalysatoren - eine <sup>57</sup>Fe mößbauerspektroskopische Studie. Dr. rer. nat., Technische Universität Berlin, Berlin
48. Bonakdarpour A, Lefevre M, Yang R, Jaouen F, Dahn T, Dodelet J-P, Dahn JR (2008) Impact of loading in RRDE experiments on Fe-



- N-C catalysts: two- or four electron oxygen reduction? *Electrochem Solid-State Lett* 11(6):B105–B108
49. Robson MH, Serov A, Atanassov P (2012) A mechanistic study of 4-aminonantipyrene and iron derived non-platinum group metal catalyst on the oxygen reduction reaction. *Electrochim Acta* 90: 656–665
  50. Leonard ND, Barton SC (2014) Analysis of adsorption effects on a metal-nitrogen-carbon catalyst using rotating ring-disk study. *J Electrochem Soc* 161(13):H3100–H3105
  51. Greenwood NN, Gibb TC (1971) Mössbauer spectroscopy, vol 1, 1st edn. Chapman and Hall Ltd., London
  52. Riedel E (1990) *Anorganische chemie*, vol 2. Walter de Gruyter, Berlin
  53. Melendres CA (1980) Mössbauer and Raman spectra of carbon-supported iron-phthalocyanine. *J Phys Chem* 84(15): 1936–1939
  54. Koslowski UI, Herrmann I, Bogdanoff P, Barkschat C, Fiechter S, Iwata N, Takahashi H, Nishikoro H (2008) Evaluation and analysis of PEM-FC performance using non-platinum cathode catalysts based on pyrolysed Fe- and Co-porphyrins—influence of a secondary heat-treatment. *ECS Trans* 13(17):125–141
  55. Roen LM, Paik CH, Jarvi TD (2004) Electrocatalytic corrosion of carbon support in PEMFC cathodes. *Electrochem Solid-State Lett* 7(1):A19–A22
  56. Sadezky A, Muckenhuber H, Grothe H, Niessner R, Pöschl U (2005) Raman microspectroscopy of soot and related carbonaceous materials: spectral analysis and structural information. *Carbon* 43(8):1731–1742
  57. Hiramitsu Y, Sato H, Hosomi H, Aoki Y, Harada T, Sakiyama Y, Nakagawa Y, Kobayashi K, Hori M (2010) Influence of humidification on deterioration of gas diffusivity in catalyst layer on polymer electrolyte fuel cell. *J Power Sources* 195:435–444